Nanobridge superconducting quantum interference devices: Beyond the Josephson limit

Dibyendu Hazra*
Department of Physics, Indian Institute of Technology Kanpur, Kanpur 208016, India

(Received 12 July 2018; revised manuscript received 10 November 2018; published 5 April 2019)

Nanoscale superconducting quantum interference devices (nano-SQUIDS) where the weak links are made from nanobridges, i.e., nanobridge SQUIDs (NBSs), are one of the most sensitive magnetometers for nanoscale magnetometry. Because of very strong nonlinearity in the nanobridge-electrode joints, the applied magnetic flux (Φ_a)–critical current (I_c) characteristics of NBSs differ very significantly from conventional tunnel-junction SQUIDs, especially when the nanobridges are long and/or the screening parameter is large. However, in most of the theoretical descriptions, NBSs have been treated as the conventional tunnel-junction SQUIDs, which are based on the dc Josephson effect. Here, I present a model demonstrating that for long nanobridges and/or large screening parameters the $I_c(\Phi_a)$ of a NBS can be explained by merely considering the fluxoid quantization in the NBS loop and the energy of the NBS; it is not necessary to take the Josephson effect into consideration. I also demonstrate that using the model, one can derive useful expressions such as the modulation depth and transfer function. I discuss the role of the kinetic inductance fraction (κ) in determining $I_c(\Phi_a)$. I compare the predictions of the present model with the experimental data already published by several groups.

DOI: 10.1103/PhysRevB.99.144505

I. INTRODUCTION

Nanoscale superconducting quantum interference devices (nano-SQUIDS) are the most sensitive magnetometers to measure the magnetic properties of individual nanoparticles or to probe the local magnetic properties of a sample in the submicron scale [1–8]. The other applications of nano-SQUIDs include measuring persistent current in a phase coherent ring [9,10], single-photon detection [11], detecting the motion of a nanomechanical oscillator [12], and as nonlinear circuit elements in quantum bits [13]. Consequently, nano-SQUIDs have been developed from versatile methods and by using different types of weak links (WLs) [6,14], such as nanobridges (NBs) [15–22], superconductor–normal-metal–superconductor proximity junctions [23–25], tunnel junctions (TJs) [26–28], and carbon nanotubes [29] to mention only a few. Out of these, NBSs have been most commonly used primarily because of their easy fabrication method [2,6].

Conventionally, a dc SQUID operation has been understood based on two phenomena: The dc Josephson effect and the fluxoid quantization in a superconducting loop [30]. An ideal dc Josephson effect predicts the flow of a lossless current—the supercurrent I_s—between two superconductors interrupted by a WL. I_s follows the relation $I_s = I_c \sin(\theta)$, where I_c is the critical current and θ is the phase of the WL. This relation holds provided most of the phase difference across the superconductor-WL-superconductor drops between the WL, resulting in a well-defined phase of the WL, for instance, as it occurs in TJs [31,32]. In the case of a NB, the phase of the bridge is not well defined in most of the cases [15,31,33]. The ideal Josephson relation in NBs, therefore, only manifests in limiting cases, e.g., where the bridge dimensions are smaller than the temperature dependent Ginzburg-Landau coherence length [$\xi(T)$] [15,31,32].

Consequently, in nanobridge SQUIDs (NBSs), various features in the $I_c(\Phi_a)$ have been observed—for instance, triangular-shaped [15,20,21,34–44], double-branched [15,34–38,40,45], and a diamond-shaped $I_c(\Phi_a)$ [15,21,35,45]—which are not conceivable by a conventional dc SQUID theory [6,30]. Thus, alternative theories [15,46] have been developed which describe some of the features, such as the nonsinusoidal $I_c(\Phi_a)$.

Here, I present a model that explains all of the above-mentioned experimental features. More importantly, unlike the previous models, here, I demonstrate that for a NBS with long NBs and/or large screening parameter, the fluxoid quantization in the NBS loop and the energy of the NBS can explain all the experimental features of $I_c(\Phi_a)$, without considering the Josephson effect. Moreover, the model presented here derives the expression for modulation depth and transfer function. I also make a quantitative comparison between the predictions of the present model and already published data by several groups demonstrating that NBSs made from niobium (Nb), niobium nitride (NbN), and lead (Pb) indeed follow the predictions of the present model.

II. MODEL OF A NANOBRIDGE SQUID BEYOND THE JOSEPHSON LIMIT

I start by presenting a qualitative comparison between a TJ and a NB—how the phase (Θ) of the superconducting order parameter is distributed in these two cases, in the presence of a finite I_s. In presence of a finite I_s, Θ is spatially nonuniform and the phase gradient is related to the supercurrent density (j_s) and the Cooper-pair density (n_s), $\nabla\Theta \propto j_s/n_s$ [32]. In a TJ, the insulating layer has negligible Cooper-pair density, $n_s \to 0$, and most of the Θ drops across the insulating layer,

*iamdibyenduhazra@gmail.com

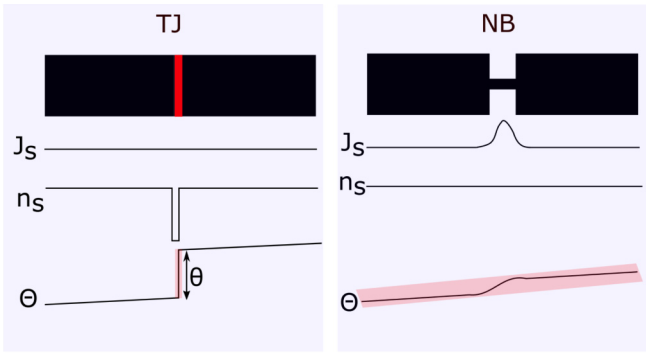

FIG. 1. Schematics showing the spatial distribution of supercurrent density j_s, Cooper-pair density n_s, and phase Θ for a tunnel junction (TJ) and for a nanobridge (NB). In the case of a TJ, there is a sharp drop of Θ across the junction, making θ well defined. In the case of a NB, Θ spreads almost uniformly across the whole structure, resulting in a poorly defined θ.

yielding a well-defined θ, as depicted schematically in Fig. 1. In the case of a NB, the bridge and the electrodes being made of the same superconductors, n_s is almost the same in NBs and in the electrodes. The enhancement of the phase gradient in the NB is a result of the enhancement of j_s due to the smallness of the width of the NB in comparison to the adjacent electrodes. In practical NBSs, the width of the NB is made typically ~2–3 times smaller than the adjacent electrodes (much wider electrodes are not desirable in order to avoid vortex penetration). Moreover, for a long NB, i.e., when the NB is longer than $\xi(T)$, j_s increases smoothly near the NB-electrode joint [31]. Altogether, in a typical NB, unlike a TJ, the phase drop across the NB is of the same order as the phase drop in the electrodes, resulting in a poorly defined θ. This can also be viewed as if θ is spread beyond the NB deep inside the electrodes [15,31,33], allowing one to treat a NB just as its electrodes with a smaller critical current. In Fig. 1, I juxtapose a NB alongside a TJ in order to compare the spatial variation of j_s, n_s, and Θ in these two types of WLs schematically.

Now, let me consider a standard NBS geometry, as shown in Fig. 2. Here, I consider a symmetric NBS where both NBs have an identical critical current I_c; the asymmetric case can be straightforwardly generalized. When the NBS is biased with a dc current I_b, it splits equally into two parallel branches—a current $I_b/2$ flows across each NB. That apart, due to the fluxoid quantization in the NBS loop, another

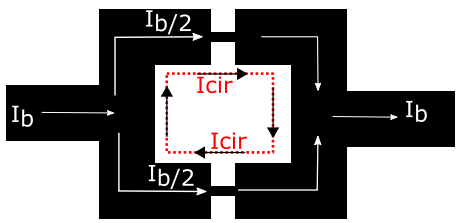

FIG. 2. Schematic of a symmetric NBS. The bias current I_b and the circulating current $I_{\rm cir}$ are shown by arrows. Here, $I_{\rm cir}$ is shown clockwise, but depending on fluxoid number n, it may also circulate counterclockwise.

current $I_{\rm cir}$ may circulate, especially in the presence of a finite Φ_a. In Fig. 2, I have schematically shown both I_b and $I_{\rm cir}$. Clearly, $I_{\rm cir}$ breaks the symmetry of the net current flow in two branches—now, the net current flowing across two NBs is $\frac{I_b}{2}+I_{\rm cir}$ and $\frac{I_b}{2}-I_{\rm cir}$, respectively. Starting from zero, with increasing I_b, depending on $I_{\rm cir}$, the net current flow across one or both the NBs will be I_c, at a particular bias current. I assume that if the net current flow across at least one of the NBs becomes I_c, it immediately switches to the voltage state—the corresponding I_b is identified as the critical current I_{cs} of the NBS. Therefore, $\frac{I_{cs}}{2}+|I_{\rm cir}|=I_c$. Rearranging, I_{cs} can be written as

$$I_{cs}=2(I_c-|I_{\rm cir}|). \tag{1}$$

Note that maximum I_{cs} is $2I_c$, i.e., when $I_{\rm cir}=0$ and the net current flowing across both the NBs is I_c.

For a given Φ_a, $I_{\rm cir}$ can be evaluated from the fluxoid quantization formula

$$L_tI_{\rm cir}+\Phi_a=n\Phi_0, \tag{2}$$

where $L_t=L_l+L_k$ is the total inductance of the NBS; L_l and L_k are the loop and kinetic inductance, respectively. The origin of the L_k is the kinetic energy due to the motion of the Cooper pairs [47,48]. n is an integer and Φ_0 is the flux quanta. The magnitude and sign (sense of circulation) of $I_{\rm cir}$ depend on n.

For a given Φ_a, n can have multiple values—the most probable n corresponds to the minimum energy (E) of the NBS which can be written as

$$E=\frac{1}{4}L_k\left[\left(\frac{I_b}{2}+I_{\rm cir}\right)^2+\left(\frac{I_b}{2}-I_{\rm cir}\right)^2\right]+\frac{1}{2}L_lI_{\rm cir}^2. \tag{3}$$

The first term within the square brackets is the kinetic energy of the Cooper pairs; the second term is the magnetic energy due to the circulation current. Moreover, to remain in the superconducting (zero-voltage) state, $|I_{\rm cir}|$ cannot exceed I_c. This imposes restrictions on n, following Eq. (2),

$$\left|\frac{n\Phi_0-\Phi_a}{L_t}\right|\leqslant I_c. \tag{4}$$

Equations (1)–(4) lay the foundation to understand $I_c(\Phi_a)$ of NBSs beyond the Josephson limit. It is convenient to express Eqs. (1)–(4) in terms of dimensionless units. I normalize currents by the maximum critical current of the NBS $I_0=2I_c$, magnetic flux by Φ_0, and the energy by $\frac{1}{4}L_kI_0^2$. With these normalizations, Eqs. (1)–(4) take the form

$$i_{cs}=(1-2|i_{\rm cir}|), \tag{5}$$

$$i_{\rm cir}=\frac{n-\phi_a}{\beta_L}, \tag{6}$$

$$\epsilon=\left[\left(\frac{i_b}{2}+i_{\rm cir}\right)^2+\left(\frac{i_b}{2}-i_{\rm cir}\right)^2\right]+2\frac{(1-\kappa)}{\kappa}i_{\rm cir}^2, \tag{7}$$

and

$$|n-\phi_a|\leqslant\frac{\beta_L}{2}, \tag{8}$$

respectively.

Here, $i_{cs}=I_{cs}/I_0$, $i_{\rm cir}=I_{\rm cir}/I_0$, $i_b=I_b/I_0$, $\phi_a=\Phi_a/\Phi_0$, $\epsilon=E/\frac{1}{4}L_kI_0^2$, $\beta_L=L_tI_0/\Phi_0=2L_tI_c/\Phi_0$, and $\kappa=L_k/L_t$. β_L

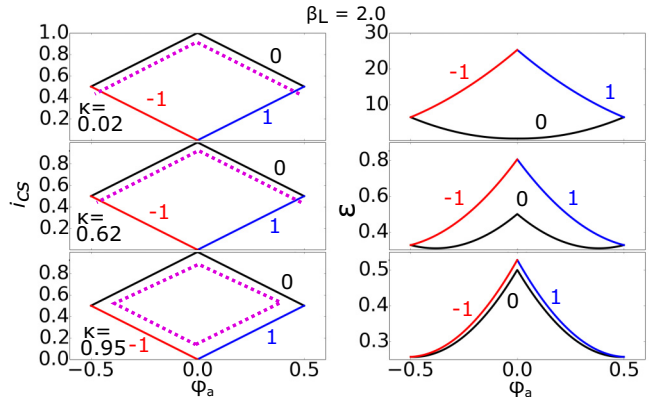

FIG. 3. Left panel: The normalized critical current i_{cs} of a NBS as a function of normalized flux ϕ_a for three different kinetic inductance fractions κ. All possible i_{cs} branches, corresponding to different allowed fluxoid numbers n, as per Eq. (8), are shown. The values of n are represented by different colors: black (0), red (-1), and blue (1), and also indicated in the figures. The expected experimental i_{cs}'s are indicated by dashed lines. All three curves are for the same screening parameter $\beta_L = 2.0$. The right panel corresponds to the normalized energy ϵ for the identical parameters of the left panel.

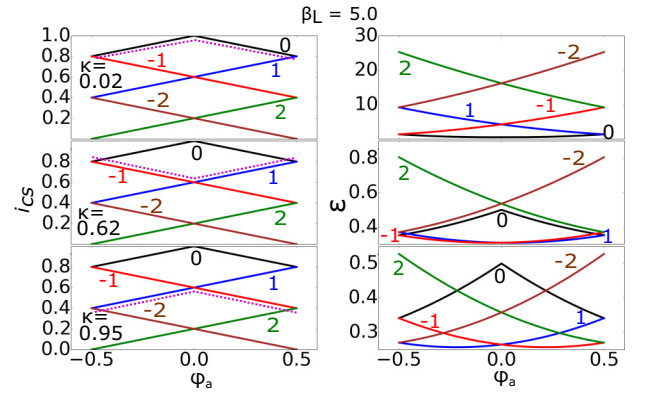

FIG. 4. Left panel: The normalized critical current i_{cs} of a NBS as a function of normalized flux ϕ_a for different kinetic inductance fractions κ. All possible i_{cs} branches, corresponding to different allowed fluxoid numbers n, as per Eq. (8), are shown. The values of n are represented by different colors: black (0), red (-1), blue (1), green (2), and brown (-2), and also indicated in the figures. The expected experimental i_{cs}'s are indicated schematically by dashed lines. All three curves are for the same screening parameter $\beta_L = 5.0$. The right panel corresponds to the normalized energy ϵ for the identical parameters of the left panel.

is the well-known screening parameter and κ is the kinetic inductance fraction, $0 \leqslant \kappa \leqslant 1$. Here, instead of L_l/L_k, I have preferred to express energy in terms of κ, as this is commonly used in the literature (see, e.g., Ref. [49] and references therein).

III. RESULTS, ANALYSIS, AND DISCUSSION

A. Variation of i_{cs} and ϵ as a function of ϕ_a

In this section, first I analyze the variation of $i_{cs}(\phi_a)$ and $\epsilon(\phi_a)$, for different values of β_L and κ. In Fig. 3, I show the variation of $i_{cs}(\phi_a)$ and $\epsilon(\phi_a)$ for $\beta_L = 2.0$ and for three different κ. Since, I_{cs} is periodic in Φ_0, i.e., i_{cs} is periodic in 1, ϕ_a is restricted in the range $-0.5 \leqslant \phi_a \leqslant 0.5$. For this particular β_L, Eq. (8) suggests that the allowed n are $n = 0$ for the entire range of ϕ_a, $-0.5 \leqslant \phi_a \leqslant 0.5$, and 1 and -1 for positive and negative flux axes, respectively. The corresponding i_{cs} are plotted in different colors, as indicated in the figure by solid lines. For this particular β_L, therefore, a maximum of two I_c branches are possible. Out of these two, to understand whether only one or both should be observable in an experiment, I also plot the corresponding ϵ on the right-hand panel, keeping in mind that the probability to occupy the lowest-energy branch is more than the higher one. For a given ϕ_a, to determine the threshold energy difference $\Delta\epsilon_{\rm th}$ between two branches below which both the I_{cs} branches should be experimentally observable, one requires a detailed thermodynamical analysis, which is not the aim of this paper. Instead, first I shall analyze the expected experimental $i_{cs}(\phi_a)$ qualitatively and subsequently discuss whether a single- or double-branched $i_{cs}(\phi_a)$ would appear for an arbitrarily chosen $\Delta\epsilon_{\rm th}$.

Returning to Fig. 3, for $\kappa = 0.02$ and 0.62, we note that the energy is always much smaller for $n = 0$ in comparison to $n = 1$ and -1, except at the boundary, $\phi_a = \pm 0.5$. Thus, in this case, the probability of an $n = 0$ configuration is much more than $n = 1$ and -1 for the entire range of $-0.5 < \phi_a < 0.5$. Thus, in $i_{cs}(\phi_a)$, experimentally, only the $n = 0$ branch should be observable, with maxima at $\phi_a = 0$, as has been observed quite commonly in several experiments, for instance, in Refs. [15,20,21,34–44]. The above scenario, quite interestingly, changes for $\kappa = 0.95$. In this case, the energy is almost the same for $n = 0$ and 1 or -1. Thus, in $i_{cs}(\phi_a)$, experimentally, all three n (0, -1, and $+1$) are accessible, and $i_{cs}(\phi_a)$ should look diamond shaped, as has been observed, for instance, in Refs. [15,21,35,45]. We note that the energy difference $\Delta\epsilon_{\rm th}$ between two branches becomes smaller and smaller as we move from the center, i.e., at $\phi_a = 0$, towards the edges, i.e., $\phi_a = \pm 0.5$. Thus, the possibility of a double-valued $i_{cs}(\phi_a)$ near $\phi_a = \pm 0.5$ is more than near $\phi_a = 0$, leading to an incomplete-diamond-shaped $i_{cs}(\phi_a)$, as has been observed, for instance, in Refs. [34,36–38,40].

With increasing β_L, more features appear. In Fig. 4, I show the variation of $i_{cs}(\phi_a)$ and $\epsilon(\phi_a)$ for $\beta_L = 5.0$ for three different κ, identical to the ones chosen in Fig. 3. For this particular β_L, the allowed n are 0, ± 1, and ± 2 for the entire range of ϕ_a. Thus, as the figures indicate, five $i_{cs}(\phi_a)$ branches are possible, in principle. Here, I would like to mention that experimentally, to the best of my knowledge, more than two branches of $i_{cs}(\phi_a)$ have not been observed in NBSs [6]. This indicates that the probability to occupy the third or any of the higher branches is very small. Following the above discussion, i.e., the $\beta_L = 2.0$ case, here also we can qualitatively understand whether one or two branches of $i_{cs}(\phi_a)$ is likely to be observed in experiments. Instead, I shall discuss the other important salient features, assuming that only single-branched $i_{cs}(\phi_a)$, corresponding to the minimum energy, is observable. For $\kappa = 0.02$, $n = 0$ corresponds to minimum energy and accordingly we get a $i_{cs}(\phi_a)$ with maxima at $\phi_a = 0$. The scenario changes quite dramatically for $\kappa = 0.62$. In this case, $n = 1$ and -1 correspond to the minimum energy for the positive and negative flux axes, respectively. Accordingly, we

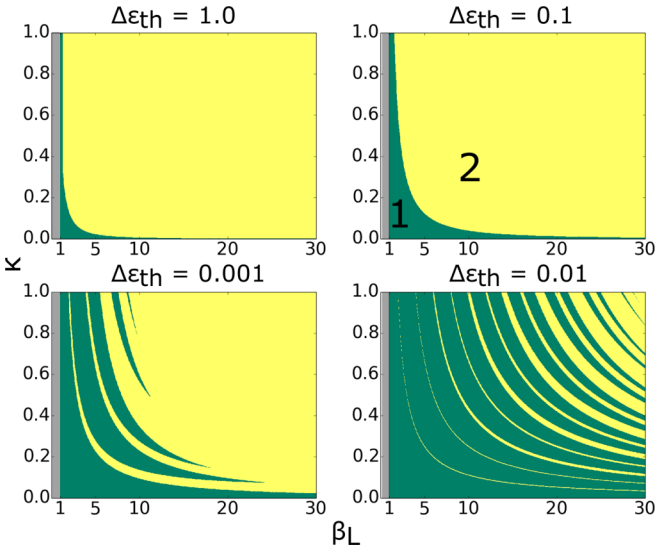

FIG. 5. The possibility of single- or double-branched $i_{cs}(\phi_a)$ of NBSs for different choices of threshold energy $\Delta\epsilon_{\rm th}$. The green color represents single-branched (also indicated by 1) whereas the yellow color represents double-branched (also indicated by 2) $i_{cs}(\phi_a)$. The gray area, $\beta_L < 1$, is within the Josephson limit and yields single-branched $i_{cs}(\phi_a)$.

get a single-branched $i_{cs}(\phi_a)$ with minima at $\phi_a = 0$. So, we see that, even for a symmetric NBS, $\phi_a = 0$ can correspond to minima of i_{cs}. This has been experimentally observed, for instance, in Refs. [21,41,45]. The scenario turns even more dramatic for $\kappa = 0.95$. Here, as $\kappa = 0.62$, the minimum energy is governed by $n = \pm 1$, but $n = -1$ corresponds to the minimum energy for the positive flux axis whereas $n = 1$ corresponds to the minimum energy for the negative flux axis. Accordingly, we get a single-branched $i_{cs}(\phi_a)$ with maxima at $\phi_a = 0$. It therefore recovers the $i_{cs}(\phi_a)$ pattern of the $\kappa = 0.02$ case, despite the fact that different n are stabilized in these two cases. Here, I would like to point out that ever since the celebrated Little-Parks experiment [50], the fluxoid quantization in a superconducting loop has been extensively studied (see, e.g., Refs. [51–54]). However, in most of the studies, the focus has been the nearest fluxoid quanta, due to the small screening parameter.

B. Determining whether single- or double-branched $i_{cs}(\phi_a)$ should be observable

From Figs. 3 and 4, it is apparent that depending upon the values of β_L and κ, $i_{cs}(\phi_a)$ can be single or double branched. In this section, I determine which combinations of β_L and κ yield single-branched and which ones yield double-branched $i_{cs}(\phi_a)$. To do so, I calculate the energy difference $\Delta\epsilon$ between the first two branches, close to the edge (i.e., $\phi_a = \pm 0.5$), at an arbitrarily chosen $\phi_a = \pm 0.35$. I assume that $\Delta\epsilon \leqslant \Delta\epsilon_{\rm th}$ yields double-branched, otherwise it leads to single-branched $i_{cs}(\phi_a)$. In Fig. 5, I show the possibility of single- or double-branched $i_{cs}(\phi_a)$ for four different choices of $\Delta\epsilon_{\rm th}$ (1.0, 0.1, 0.01, and 0.001, respectively) as a function of β_L and κ. We see that for $\beta_L \to 1$, irrespective of the values of κ and for $\kappa \to 0$, irrespective of the values of β_L, yield single-branched $i_{cs}(\phi_a)$, independent of the choices of $\Delta\epsilon_{\rm th}$. For $\Delta\epsilon_{\rm th} = 1$ and 0.1, at a fixed β_L, higher κ values increase the probability of double-branched $i_{cs}(\phi_a)$. In these cases, the most of the area in the β_L-κ space favors the double-branched $i_{cs}(\phi_a)$. With decreasing $\Delta\epsilon_{\rm th}$, β_L-κ space is divided into different domains: Certain combinations of β_L and κ favor single- and the remaining combinations favor double-branched $i_{cs}(\phi_a)$. Furthermore, with decreasing $\Delta\epsilon_{\rm th}$, more and more of the area of β_L-κ space favors single-branched $i_{cs}(\phi_a)$. Also note that with increasing β_L and κ, the area of the double-branched $i_{cs}(\phi_a)$ domains increases. For materials with higher κ, such as niobium and niobium nitride [55], typically also have a higher critical current density compared to materials with lower κ, for instance, Al. Thus, for identical NBS geometries, β_L is also higher for high-κ materials, making the appearance of double-branched $i_{cs}(\phi_a)$ more probable compared to low-κ ones, as has been reported in several publications, for instance, in Refs. [15,34,35,40,45].

C. Calculating modulation depth and transfer function

In this section, I shall calculate two important parameters, namely, the modulation depth and the transfer function. For simplicity, first let me consider the case where only $n = 0$ is accessible. From Eq. (5), it is clear that maximum i_{cs}, $i_{cs}^{\rm max}$, corresponds to minimum $|i_{\rm cir}|$ whereas minimum i_{cs}, $i_{cs}^{\rm min}$, corresponds to maximum $|i_{\rm cir}|$. For $n = 0$, Eq. (6) suggests that minimum $|i_{\rm cir}|$ is 0 whereas maximum $|i_{\rm cir}|$ is $0.5/\beta_L$ (corresponding to $\phi_a = 0$ and ± 0.5, respectively). This leads to $i_{cs}^{\rm max} = 1$ and $i_{cs}^{\rm min} = 1 - 1/\beta_L$, yielding a modulation depth

$$i_{cs}^{\rm max} - i_{cs}^{\rm min} = \frac{I_{cs}^{\rm max} - I_{cs}^{\rm min}}{I_0} = \frac{1}{\beta_L}, \tag{9}$$

in normalized scale.

It can be shown that Eq. (9) is valid in general, irrespective of whether $i_{cs}(\phi_a)$ is single or double branched. This is also evident from both Figs. 3 and 4. Here, I would like to point out that Eq. (9) can be derived approximately from conventional dc SQUID theory [6,30] and has often been used in the context of NBSs.

For the transfer function ($I_{cs\Phi_a}$), i.e., the slope of the $i_{cs}(\phi_a)$, since the variation of $i_{cs}(\phi_a)$ is linear, $I_{cs\Phi_a}$ can straightforwardly be derived as

$$I_{cs\Phi_a} = \frac{I_{cs}^{\rm max} - I_{cs}^{\rm min}}{\Phi_0/2} = \frac{2I_0}{\beta_L \Phi_0}. \tag{10}$$

D. Comparison with the existing models

In this section, I compare the present model with conventional dc SQUID theory [30] as well as two previous models for NBSs [15,46]. The conventional dc SQUID theory is based on an ideal Josephson effect which assumes a well-defined phase and a sinusoidal relation between the supercurrent and phase of the junction. This assumption is not valid for NBs, especially when they are longer than $\xi(T)$ [15,31]. Consequently, conventional dc SQUID theory cannot explain the triangular-shaped $i_{cs}(\phi_a)$. To demonstrate this, in Fig. 6, I plot $i_{cs}(\phi_a)$ of a conventional dc SQUID for different values of β_L. For comparison, I also plot $i_{cs}(\phi_a)$, as predicted from the present model, assuming a single-branched $i_{cs}(\phi_a)$. Clearly, at

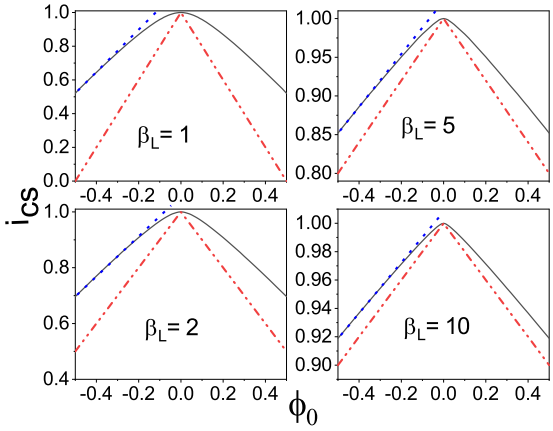

FIG. 6. Comparison of the present model (dashed lines) with the conventional dc SQUID theory (solid lines) for different values of β_L. The dotted straight lines on the conventional dc SQUID curves demonstrate that near $\phi_a = 0$, irrespective of the values of β_L, $i_{cs}(\phi_a)$ deviates from the linear variation.

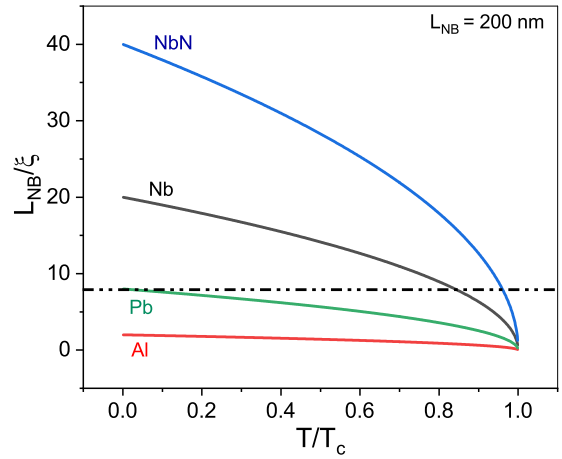

FIG. 7. The temperature dependence of $L_{\rm NB}/\xi(T)$ for a typical $L_{\rm NB} = 200$ nm. The horizontal line represents $L_{\rm NB}/\xi(T) = 8.0$, above which, according to Podd *et al.* [46], a NB behaves as an infinitely long superconducting wire.

large β_L, the $i_{cs}(\phi_a)$ prediction from the conventional theory tends to match with the present model. Moreover, note that, near the half-flux quanta, irrespective of the values of β_L, the conventional dc SQUID theory shows a linear $i_{cs}(\phi_a)$, whereas near the integer flux quanta, it deviates from the linear behavior. Another important point worth mentioning here is that the conventional dc SQUID theory does not provide an explanation for a double-branched and/or diamond-shaped $i_{cs}(\phi_a)$.

Here, I would like to point out that for most of the Nb-, Pb-, or NbN-based NBSs reported in the literature, which show linear $i_{cs}(\phi_a)$, have β_L in the range ∼5–30, due to their high critical current density and large kinetic inductance. On the other hand, Al-based NBSs, which show sinusoidal $i_{cs}(\phi_a)$, have $\beta_L \sim 1$ due to their low critical current density and small kinetic inductance. It therefore appears that at low β_L, typically below ∼2, $i_{cs}(\phi_a)$ of a NBS is better described by the conventional dc SQUID theory.

Hasselbach *et al.* [15] developed a model for NBSs by extensively solving the Ginzburg-Landau (GL) equation in two-dimensional (2D) NBS structures. This model, as the present model, can explain the triangular-shaped $i_{cs}(\phi_a)$ characteristics in the long junction limit. However, in this model, the authors did not take into account the different fluxoid states and the energy of the NBSs. Consequently, it cannot explain for a double-branched and/or a diamond-shaped $i_{cs}(\phi_a)$.

Podd *et al.* [46] developed a one-dimensional model for NBSs. However, the authors assumed a well-defined phase of the NB, which contradicts the findings of Refs. [15,31]. Also, the authors did not take into account the different fluxoid states and the energy of the NBS. Consequently, it too cannot explain for a double-branched and/or a diamond-shaped $i_{cs}(\phi_a)$.

E. Spatial variation of the phase of the NBs: Material choice and temperature range

The central assumption of the present model is that the phase drop across the NBs is not significantly higher than the overall phase drop across the electrodes, as depicted schematically in Fig. 1. By solving 2D GL equations, Hasselbach *et al.* [15] has shown that a sharp phase drop across the NB takes place only when the NB is significantly shorter than $\xi(T)$. On the other hand, as the NB becomes longer than $\xi(T)$, the phase of the NB starts spreading inside the electrode. Typically, for NB longer than $3\xi(T)$, the current-phase relation becomes linear, resulting in a triangular $i_{cs}(\phi_a)$ characteristic. Podd *et al.* [6,46], by solving 1D GL equations, demonstrated that when the NB is longer than $8\xi(T)$, the critical current is independent of the length of the NB and is equal to the depairing current of an infinitely long superconducting wire. In other words, according to Podd *et al.* [46], when the NB is longer than $8\xi(T)$, it's phase can be disregarded.

Based on these findings, now let me analyze whether one can disregard the phase of the NBs in a NBS, made from two most commonly used materials, Nb and Al. For completeness, I also include Pb [41] and NbN [45] which have also been reported in the literature. In Fig. 7, I show the variation of $L_{\rm NB}/\xi(T)$ as a function of normalized temperature T/T_c for NBs with a typical NB length of 200 nm (see Table I). The bulk ξ_0 are ∼1600, 40, 80, and 10 nm, respectively, for Al, Nb, Pb, and NbN. However, in a thin-film configuration, due to the reduced mean free path, the effective ξ_0 is reduced considerably. Taking the numbers reported in the literature, ξ_0's are chosen as 100, 10, 25, and 5 nm, respectively, for Al [15], Nb [56], Pb [57], and NbN [58,59] thin films. For the temperature dependence, I use the expression $\xi(T) = \xi(0)/\sqrt{1 - T/T_c}$ [32]. The graph shows that except for very close to T_c, for Nb, Pb, and NbN, $L_{\rm NB}$ remains quite larger than $\xi(T)$. Consequently, the phase of the NBs can be disregarded except for close to T_c. For Al, on the other hand, $L_{\rm NB}$ is always close to $\xi(T)$. Hence, the phase drop across the NBs is more significant. Here, I would like to point out that using a modern electron beam lithography technique, it is possible to reduce $L_{\rm NB}$ below 50 nm. However, Nb, Pb, and NbN also have very high critical current densities which further increase

TABLE I. Summary of the various parameters. Here, L_{NB} is the length and W_{NB} is the width of the NBs. d is the thickness of the films. $N_\square$ is the number of the square contributing to the kinetic inductance. I_{cs}^{max} is the maximum observed critical current of the NBSs, ΔI_{cs} is the modulation depth, N is the number of observed branches in $i_{cs}(\phi_a)$, β_L is the screening parameter, κ is the kinetic inductance fraction, and λ_{eff} is the effective magnetic penetration depth.

NBS material	L_{NB} (nm)	W_{NB} (nm)	d (nm)	$N_\square$	I_{cs}^{max} (μA)	ΔI_{cs} (μA)	N	β_L	κ	λ_{eff} (nm)	Adopted from Ref.
Nb	184	100	30	16	2022.5	94.3	2	21.4	0.93	169.5	[15]
Nb	300	30	30	15	662.0	37.0	2	17.9	0.97	192	[34]
W-Nb-Al	180	40	80-25-20	43	17.5	1.5	2	11.9	0.99	802	[21]
Nb	280	120	30	15	500	100	1	5	0.93	174	[62]
NbN	120	50	30	18	67	2.5	2	26.8	0.99	884	[45]
NbN	120	50	20	18	26	1.4	1	18.6	0.99	965	[45]
Cr-Pb-Cr	350	80	5-40-8	21	1778	203.5	1	8.74	0.86	115	[41]

with decreasing length, resulting in an undesirably large Joule heating while switching to the voltage state [60,61].

It is quite clear from the above discussion that for identical geometry, the phase is more robustly defined for NBs made from the materials with longer ξ compared to the materials with shorter ξ. Consequently, $i_{cs}(\phi_a)$ of NBSs made from the materials with longer ξ closely follows the predictions of conventional dc SQUID theory compared to the materials with shorter ξ. In other words, $i_{cs}(\phi_a)$ of NBSs made from the materials with longer ξ is more nonlinear compared to materials with shorter ξ. On the other hand, Fig. 6 indicates that lower β_L yields more nonlinearity in the $i_{cs}(\phi_a)$ of NBSs. Therefore, for identical NBS geometry, longer ξ should lead to lower β_L and vice versa. To verify this, we note that, for most of the NBSs, $L_k \gg L_g$, i.e., $\kappa \sim 1$ (see Table I). Thus, $\beta_L \propto L_k I_c$. I_c, for a long NB, varies as $I_c \propto 1/(\lambda^2 \xi)$ [32] whereas L_k varies as $L_k \propto \lambda^2$, resulting in $\beta_L \propto 1/\xi$.

IV. COMPARISON WITH EXPERIMENTS

In this section, I provide a quantitative comparison between the predictions from the present model with the experimental data already published by several groups.

A. Shape of $i_{cs}(\phi_a)$

It appears from the discussion of the previous section that the shape of $i_{cs}(\phi_a)$ for a Nb NBS is expected to follow the present model whereas an Al NBS should show significant deviation. To verify this, first we compare experimental data, adopted from Hasselbach *et al.* [15] who studied temperature-dependent $i_{cs}(\phi_a)$ for both Al and Nb NBSs. In Fig. 8, I plot $i_{cs}(\phi_a)$ and check whether it follows the linear variation predicted from the present model. The Al NBS has a diameter $\sim$1.25 μm with NBs 289 nm long and 66 nm wide and the arms are 237 nm wide. The Nb NBS has a diameter $\sim$1.25 μm with NBs 184 nm long and 100 nm wide and the arms are 285 nm wide. The graph clearly shows that for the Al NBS there is a clear departure from the linear variation whereas for the Nb NBS there is indeed a linear variation. As Nb, the linear (triangular) $i_{cs}(\phi_a)$ have also been observed for Pb [41] and NbN [45] NBSs. For Al NBSs, the departures from the linear variation of $i_{cs}(\phi_a)$ have also been observed by other groups, e.g., see Vijay *et al.* [19].

B. Comparing ΔI_{cs}

According to the present model, $\Delta I_{cs} = \Phi_0/(L_g + L_k)$. L_g can be estimated from the geometry (also reported in the referred papers of Table I). L_k is related to the effective penetration depth λ_{eff} [55], $L_k = N_\square \mu_0 \lambda_{eff}^2/d$, where d is the thickness and $N_\square$ is the number of squares contributing to the kinetic inductance, μ_0 is the free-space permeability, and d is the thickness of the films. $N_\square$ can be estimated from the geometry. Thus, the only unknown parameter is λ_{eff}. Since λ_{eff} depends on d and is also very susceptible to the detailed deposition method, condition, and parameters, it is difficult to estimate λ_{eff} for the particular reported sample. Thus, from the known values of ΔI_{cs}, I extract λ_{eff} at low temperatures for NBSs reported in the literature (see Table I) and compare whether the extracted λ_{eff} is in the expected range. In Table I, I summarize the geometry of the NBSs and report the extracted λ_{eff} at the lowest temperature.

For Nb NBSs, the extracted λ_{eff} is in the range 170–190 nm. This is close to $\lambda_{eff}(0) \sim 140$ nm measured by Gubin *et al.* [63] for 30-nm-thin Nb film. For trilayer W-Nb-Al NBS [21], the extracted λ_{eff} ($\sim$800 nm) is much higher than the usual value. This may be due to the increased disorder because of the presence of a thick W layer underneath. This is also evident from the fact that the trilayer W-Nb-Al film has very low $T_c \sim 2$ K in comparison to 30-nm-thin Nb films, $T_c \sim 8$ K. For NbN, we extract $\lambda_{eff}(0) \sim 900$ nm which is of the same order ($\sim$500 nm) of what is reported by Kamlapure *et al.* [64]. The remaining discrepancy may be due to the fact that while estimating $N_\square$, I have only considered the NBS loop area, though a significant contribution may come

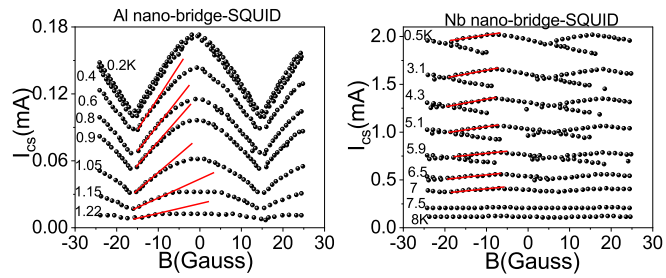

FIG. 8. The variation of I_{cs} as a function of applied magnetic field (B) at different temperatures for Al and Nb NBSs. The solid lines represent straight lines. The data are adopted from Ref. [15].

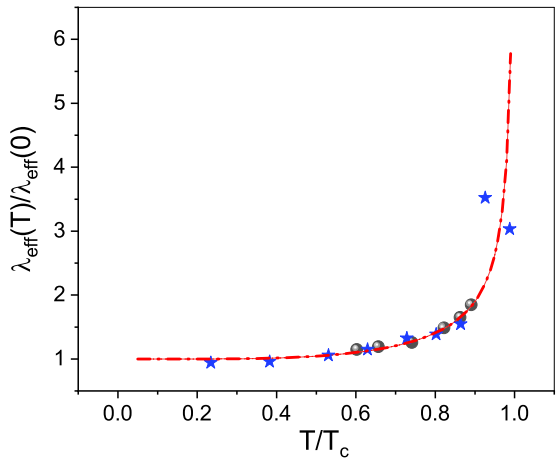

FIG. 9. The variation of $\lambda_{\rm eff}(T)/\lambda_{\rm eff}(0)$ for Nb (blue star) and Pb (black dot) NBSs. The solid line is a fit with the BCS theory. The data are extracted from Refs. [15,41], respectively.

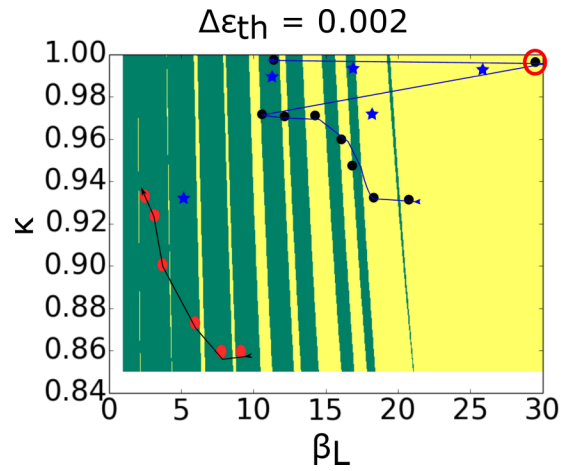

FIG. 10. Number of branches: Comparison between theory and experiments. The theoretical color plot is for $\Delta\epsilon_{\rm th} = 0.002$ and the color code is identical to Fig. 5. (β_L, κ) points are adopted from Ref. [15] (black dots) and Ref. [41] (red oval). The solid lines are guide for eyes. The arrows show the direction of the increasing temperature. The stars show the (β_L, κ) points from Table I for the remaining references. The circle shows the data point where there is a mismatch between theory and experiment.

from the other portion of the NBSs, especially for a high-κ material such as NbN [55,65]. Moreover, for a disordered material such as NbN, the superconducting parameters are very susceptible to disorder and therefore depend very significantly on the exact deposition method [58,66,67]. For Pb, the extracted $\lambda_{\rm eff}$ is close to what is reported by Ozer *et al.* [57], ∼145 nm.

In most of the studies, $i_{cs}(\phi_a)$ have been reported at the lowest measuring temperature, allowing to estimate $\lambda_{\rm eff}$ only at a particular temperature. However, Hasslbach *et al.* [15] and Paul *et al.* [41] have reported temperature-dependent $i_{cs}(\phi_a)$ for Nb and Pb NBSs, respectively, allowing to see how $\lambda_{\rm eff}$ evolves with the temperature and verify whether they are consistent with the dirty limit BCS expression [32],

$$\frac{\lambda_{\rm eff}(T)}{\lambda_{\rm eff}(0)} = \frac{1}{\sqrt{\delta(T)\tanh\left[\beta\delta(T)\frac{T_c}{T}\right]}}, \tag{11}$$

where $\delta(T) = \Delta(T)/\Delta(0)$ is the normalized energy gap and $\beta = \Delta(0)/2k_BT_c$. In Fig. 9, I fit the data extracted from Hasslbach *et al.* [15] and Paul *et al.* [41] with Eq. (11), taking $\lambda_{\rm eff}(0)$ as a fit parameter. The fit is quite good and I extract $\lambda_{\rm eff}(0) = 180$ nm for Nb and 120 nm for Pb NBSs, which are close to the numbers reported in the literature, as has already been mentioned in the previous section.

C. Tracing the number of branches

In this section, I explore the number of branches (N) observed in experiments and compare them with the prediction from the present model. In Table I, I summarize the N as observed at the lowest measuring temperature by different groups. Moreover, Hasselbach *et al.* [15] and Paul *et al.* [41] have reported temperature-dependent $i_{cs}(\phi_a)$ that give additional data points. β_L is estimated from $L_t \times I_{cs}^{\rm max}/\Phi_0$. In Fig. 10, I show the experimental (β_L, κ) data points on the color map of the theoretical prediction from the present model. $\Delta\epsilon_{\rm th}$ is intuitively chosen as 0.002 to be consistent with the most number of data points. Taking a typical error bar ∼25% for both β_L and κ, except for one data point highlighted by the circle, the experimentally observed N matches well with the prediction from the present model. A complete match is not expected as $\Delta\epsilon_{\rm th}$ is arbitrarily chosen and it might also have a temperature dependence.

V. SUMMARY AND CONCLUSION

In summary, I have developed a model for NBSs beyond the Josephson limit, i.e., for long NBs and/or large screening parameter. In this limit, the $i_{cs}(\phi_a)$ of a NBS can be understood by considering the fluxoid quantization in the NBS loop and the energy of the NBS. The model explains various experimental features, such as triangular-shaped, double-branched, and a diamond-shaped $I_c(\Phi_a)$, reported in the literature. From the model, I derive the expression for the modulation depth and the transfer function. Using the model, I have shown that both the screening parameter and the kinetic inductance fraction play a vital role in deciding the number of $i_{cs}(\phi_a)$ branches. I compare the prediction of the model with the experimental data, already published by several groups, on Al, Nb, NbN, and Pb NBSs. As expected, the shape of the $I_c(\Phi_a)$ for Al NBSs shows a significant departure from the predictions of the present model whereas the NBSs made from the remaining materials show good agreement. Likewise, the present model also makes a good prediction about the number of $I_c(\Phi_a)$ branches for an arbitrarily chosen $\Delta\epsilon_{\rm th}$. In future, it will be interesting to calculate $\Delta\epsilon_{\rm th}$ as well as to see whether it depends on the material properties and whether it has a temperature and magnetic field dependence.

ACKNOWLEDGMENT

I acknowledge the financial support in the form of scholarship from the Council of Scientific & Industrial Research (CSIR), the government of India.

[1] W. Wernsdorfer, Classical and quantum magnetization reversal studied in nanometer-sized particles and clusters, *Handbook of Advanced Magnetic Materials*, edited by Y. Liu, D. J. Sellmyer, and D. Shindo (Springer, Boston, MA, 2006), pp. 77–127.

[2] W. Wernsdorfer, Supercond. Sci. Technol. **22**, 064013 (2009).

[3] C. Foley and H. Hilgenkamp, Supercond. Sci. Technol. **22**, 064001 (2009).

[4] D. Vasyukov, Y. Anahory, L. Embon, D. Halbertal, J. Cuppens, L. Neeman, A. Finkler, Y. Segev, Y. Myasoedov, M. L. Rappaport *et al.*, Nat. Nanotechnol. **8**, 639 (2013).

[5] E. Levenson-Falk, R. Vijay, N. Antler, and I. Siddiqi, Supercond. Sci. Technol. **26**, 055015 (2013).

[6] C. Granata and A. Vettoliere, Phys. Rep. **614**, 1 (2016).

[7] J. Gallop and L. Hao, ACS Nano **10**, 8128 (2016).

[8] G. Yue, L. Chen, J. Barreda, V. Bevara, L. Hu, L. Wu, Z. Wang, P. Andrei, S. Bertaina, and I. Chiorescu, Appl. Phys. Lett. **111**, 202601 (2017).

[9] D. Mailly, C. Chapelier, and A. Benoit, Phys. Rev. Lett. **70**, 2020 (1993).

[10] W. Rabaud, L. Saminadayar, D. Mailly, K. Hasselbach, A. Benoit, and B. Etienne, Phys. Rev. Lett. **86**, 3124 (2001).

[11] L. Hao, J. Gallop, C. Gardiner, P. Josephs-Franks, J. Macfarlane, S. Lam, and C. Foley, Supercond. Sci. Technol. **16**, 1479 (2003).

[12] S. Etaki, M. Poot, I. Mahboob, K. Onomitsu, H. Yamaguchi, and H. van der Zant, Nat. Phys. **4**, 785 (2008).

[13] R. Vijay, J. D. Sau, M. L. Cohen, and I. Siddiqi, Phys. Rev. Lett. **103**, 087003 (2009).

[14] M. J. Martínez-Pérez and D. Koelle, Phys. Sci. Rev. **2**, 20175001 (2017).

[15] K. Hasselbach, D. Mailly, and J. Kirtley, J. Appl. Phys. **91**, 4432 (2002).

[16] S. Lam and D. Tilbrook, Appl. Phys. Lett. **82**, 1078 (2003).

[17] A. G. Troeman, H. Derking, B. Borger, J. Pleikies, D. Veldhuis, and H. Hilgenkamp, Nano Lett. **7**, 2152 (2007).

[18] L. Hao, J. Macfarlane, J. Gallop, D. Cox, J. Beyer, D. Drung, and T. Schurig, Appl. Phys. Lett. **92**, 192507 (2008).

[19] R. Vijay, E. Levenson-Falk, D. Slichter, and I. Siddiqi, Appl. Phys. Lett. **96**, 223112 (2010).

[20] S. Mandal, T. Bautze, O. A. Williams, C. Naud, E. Bustarret, F. Omnes, P. Rodiere, T. Meunier, C. Bäuerle, and L. Saminadayar, ACS Nano **5**, 7144 (2011).

[21] D. Hazra, J. R. Kirtley, and K. Hasselbach, Appl. Phys. Lett. **103**, 093109 (2013).

[22] L. Chen, H. Wang, X. Liu, L. Wu, and Z. Wang, Nano Lett. **16**, 7726 (2016).

[23] L. Angers, F. Chiodi, G. Montambaux, M. Ferrier, S. Guéron, H. Bouchiat, and J. C. Cuevas, Phys. Rev. B **77**, 165408 (2008).

[24] A. Ronzani, M. Baillergeau, C. Altimiras, and F. Giazotto, Appl. Phys. Lett. **103**, 052603 (2013).

[25] S. Samaddar, D. Van Zanten, A. Fay, B. Sacépé, H. Courtois, and C. Winkelmann, Nanotechnology **24**, 375304 (2013).

[26] R. Wölbing, J. Nagel, T. Schwarz, O. Kieler, T. Weimann, J. Kohlmann, A. Zorin, M. Kemmler, R. Kleiner, and D. Koelle, Appl. Phys. Lett. **102**, 192601 (2013).

[27] C. Granata, A. Vettoliere, R. Russo, M. Fretto, N. De Leo, and V. Lacquaniti, Appl. Phys. Lett. **103**, 102602 (2013).

[28] M. Schmelz, V. Zakosarenko, T. Schönau, S. Anders, S. Linzen, R. Stolz, and H. Meyer, Supercond. Sci. Technol. **30**, 014001 (2016).

[29] J.-P. Cleuziou, W. Wernsdorfer, V. Bouchiat, T. Ondarçuhu, and M. Monthioux, Nat. Nanotechnol. **1**, 53 (2006).

[30] J. Clarke and A. I. Braginski, *The SQUID Handbook: Applications of SQUIDs and SQUID Systems* (Wiley, Hoboken, NJ, 2006).

[31] K. Likharev, Rev. Mod. Phys. **51**, 101 (1979).

[32] M. Tinkham, *Introduction to Superconductivity* (Courier Corporation, North Chelmsford, MA,1996).

[33] A. Gumann, T. Dahm, and N. Schopohl, Phys. Rev. B **76**, 064529 (2007).

[34] K. Hasselbach, C. Veauvy, and D. Mailly, Physica C: Superconductivity **332**, 140 (2000).

[35] M. Faucher, T. Fournier, B. Pannetier, C. Thirion, W. Wernsdorfer, J. Villegier, and V. Bouchiat, Physica C: Superconductivity **368**, 211 (2002).

[36] G. Hutchinson, H. Qin, D. Kang, S. Lee, D. Hasko, M. Blamire, and D. Williams, Supercond. Sci. Technol. **16**, 1544 (2003).

[37] G. Hutchinson, H. Qin, D. Hasko, D. Kang, and D. Williams, Appl. Phys. Lett. **84**, 136 (2004).

[38] G. Hutchinson, H. Qin, D. Kang, S. Lee, M. Blamire, D. Hasko, and D. Williams, Microelectron. Eng. **73**, 773 (2004).

[39] R. Russo, C. Granata, E. Esposito, D. Peddis, C. Cannas, and A. Vettoliere, Appl. Phys. Lett. **101**, 122601 (2012).

[40] D. Hazra, J. R. Kirtley, and K. Hasselbach, Appl. Phys. Lett. **104**, 152603 (2014).

[41] S. Paul, S. Biswas, and A. K. Gupta, Supercond. Sci. Technol. **30**, 025017 (2016).

[42] A. N. McCaughan, Q. Zhao, and K. K. Berggren, Sci. Rep. **6**, 28095 (2016).

[43] L. Wu, L. Chen, H. Wang, Q. Wang, H. Wo, J. Zhao, X. Liu, X. Wu, and Z. Wang, Supercond. Sci. Technol. **30**, 074011 (2017).

[44] S. Biswas, C. B. Winkelmann, H. Courtois, and A. K. Gupta, Phys. Rev. B **98**, 174514 (2018).

[45] R. Russo, E. Esposito, A. Crescitelli, E. Di Gennaro, C. Granata, A. Vettoliere, R. Cristiano, and M. Lisitskiy, Supercond. Sci. Technol. **30**, 024009 (2016).

[46] G. J. Podd, G. D. Hutchinson, D. A. Williams, and D. G. Hasko, Phys. Rev. B **75**, 134501 (2007).

[47] W. Henkels and C. Kircher, IEEE Trans. Magn. **13**, 63 (1977).

[48] A. Barone and G. Paterno, *Physics and Applications of the Josephson Effect* (Wiley, New York, 1982), Chap. 13.

[49] P. K. Day, H. G. LeDuc, B. A. Mazin, A. Vayonakis, and J. Zmuidzinas, Nature (London) **425**, 817 (2003).

[50] R. Parks and W. Little, Phys. Rev. **133**, A97 (1964).

[51] V. Moshchalkov, L. Gielen, M. Dhallé, C. Van Haesendonck, and Y. Bruynseraede, Nature (London) **361**, 617 (1993).

[52] J. Mooij and C. Harmans, New J. Phys. **7**, 219 (2005).

[53] S. Michotte, D. Lucot, and D. Mailly, Phys. Rev. B **81**, 100503(R) (2010).

[54] A. Sivakov, A. Pokhila, A. Glukhov, S. Kuplevakhsky, and A. Omelyanchouk, Low Temp. Phys. **40**, 408 (2014).

[55] A. J. Annunziata, D. F. Santavicca, L. Frunzio, G. Catelani, M. J. Rooks, A. Frydman, and D. E. Prober, Nanotechnology **21**, 445202 (2010).

[56] S. Bose, P. Raychaudhuri, R. Banerjee, and P. Ayyub, Phys. Rev. B **74**, 224502 (2006).

[57] M. M. Özer, J. R. Thompson, and H. H. Weitering, Nat. Phys. **2**, 173 (2006).

[58] D. Hazra, N. Tsavdaris, S. Jebari, A. Grimm, F. Blanchet, F. Mercier, E. Blanquet, C. Chapelier, and M. Hofheinz, Supercond. Sci. Technol. **29**, 105011 (2016).

[59] D. Hazra, N. Tsavdaris, A. Mukhtarova, M. Jacquemin, F. Blanchet, R. Albert, S. Jebari, A. Grimm, A. Konar, E. Blanquet *et al.*, Phys. Rev. B **97**, 144518 (2018).

[60] D. Hazra, L. M. Pascal, H. Courtois, and A. K. Gupta, Phys. Rev. B **82**, 184530 (2010).

[61] D. Hazra, J. R. Kirtley, and K. Hasselbach, Phys. Rev. Appl. **4**, 024021 (2015).

[62] C. Granata, A. Vettoliere, R. Russo, E. Esposito, M. Russo, and B. Ruggiero, Appl. Phys. Lett. **94**, 062503 (2009).

[63] A. I. Gubin, K. S. Il'in, S. A. Vitusevich, M. Siegel, and N. Klein, Phys. Rev. B **72**, 064503 (2005).

[64] A. Kamlapure, M. Mondal, M. Chand, A. Mishra, J. Jesudasan, V. Bagwe, L. Benfatto, V. Tripathi, and P. Raychaudhuri, Appl. Phys. Lett. **96**, 072509 (2010).

[65] D. Hazra, S. Jebari, R. Albert, F. Blanchet, A. Grimm, C. Chapelier, and M. Hofheinz, arXiv:1806.03935.

[66] M. Chand, Ph.D. thesis, Tata Institute of Fundamental Research, India, 2012.

[67] N. Tsavdaris, D. Harza, S. Coindeau, G. Renou, F. Robaut, E. Sarigiannidou, M. Jacquemin, R. Reboud, M. Hofheinz, E. Blanquet *et al.*, Chem. Mater. **29**, 5824 (2017).